Room temperature AC impedance and dielectric studies of Bi and Sr doped PrCo$_{0.6}$Fe$_{0.4}$O$_3$ perovskites

Unikoth Megha[1,*], George Varghese[2,*], Karakat Shijina[1]

[1]*Department of Physics, University of Calicut, Kerala-673635, India*
[2]*Research Centre, Mar Ivanios College, Thriuvananthapuram, 695015, Kerala, India*

Abstract

In this study, Bi and Sr doped PrCo$_{0.6}$Fe$_{0.4}$O$_3$ perovskites were synthesised by citrate sol-gel auto-combustion method and sintered at 900 °C. The X-ray diffraction pattern shows that all compounds have orthorhombic crystal structure with Pbnm space group and a small amount of secondary phase was observed only in the sample with higher Bi content (Pr$_{0.8}$Bi$_{0.2}$Co$_{0.6}$Fe$_{0.4}$O$_3$). The average grain sizes of the samples were below 400 nm and the corresponding elemental composition was confirmed from EDS spectra. The oxidation states of elements and the presence of oxygen vacancies were obtained from XPS spectra. The vacancies were found to be more in the Sr-doped compound. Finally, from the detailed complex impedance analysis, it was found that the grain boundary resistance is dominant at room temperature. The variation of dielectric properties and AC conductivity with frequency reveals that the relaxation process was due to Maxwell-Wagner type of interfacial polarisation.

Keywords: PrCo$_{0.6}$Fe$_{0.4}$O$_3$, doping, structural characterization, electrical properties, grain boundary effects

I. Introduction

The unusual properties of rare earth cobalties (RCoO$_3$) having perovskite structures are largely influenced by the intricate electronic spin states of Co^{3+} ion present in it. The changes in spin state of Co^{3+} due to the temperature variation affects the structural, magnetic and optical properties of these compounds [1,2]. These materials show unique properties such as orbital ordering, charge ordering, charge disproportion, colossal magnetoresistance (CMR), phase separation etc. [3–5]. Due to these fascinating properties they are frequently used as sensors, substrates, catalytic electrodes and are potential candidates in optoelectronic and spintronic applications. These compounds have common features such as high thermoelectric power, superconductivity, ferroelectricity, charge ordering and spin dependent CMR [6].

The Co^{3+} in RCoO$_3$ has 3 d^6 configuration and can exist in three spin states, low spin LS (t$_{2g}^6$ e$_g^0$), inter-mediate spin IS (t$_{2g}^5$ e$_g^1$) and high spin state HS (t$_{2g}^4$ e$_g^2$) which can induce spin isotropic effect in the perovskite structure. LaCoO$_3$ is a non-magnetic insulator in its LS ground state. It shows LS to HS phase transition in the temperature range of 50 K < T < 150 K and a metal-insulator transition at 500 K. Also, LS-LS/HS-IS scenario exists in all RCoO$_3$ compounds, which is responsible for the drastic changes in structural, electrical and magnetic properties of these compounds [7]. The double or super exchange interaction between Co^{3+} and Co^{4+} ions are responsible for the existence of ferromagnetism as well as the spin glass transitions in these compounds [8]. Ni^{3+} doped LaCoO$_3$ shows ferromagnetic nature for x > 10% and for x < 0.5 sample exhibits spin glass behaviour. Troyanchuk *et al.* [8] studied Fe doped systems and reported that for x ≥ 0.4 it has small spontaneous magnetic moment and at T$_N$ = 120 K it becomes fully paramagnetic. Fe stabilises the Co ions in the low spin state. The cell parameter of LaCo$_{1-x}$Fe$_x$O$_3$ increases linearly with the Fe addition which favours the low spin of the Co ions. Fe incorporation weakens Co–O bond in CoO$_6$ octahedra and near the oxygen vacancies Co^{2+} and Co^{3+} have HS state causing single ion mag-

---
*Corresponding author: tel: +91 90 48029 595 ,
e-mail: *meghaunikoth@gmail.com,* (U. Megha)
e-mail: *gv@uoc.ac.in* (G. Varghese)

netic anisotropy. Weak ferromagnetism and large magnetic anisotropy are the main characteristics of the Fe doped systems [9,10].

Similar to $LaCoO_3$, $PrCoO_3$ in its ground state has no magnetic ordering due to the low spin state of Co^{3+} ions [11]. It was reported that it shows high-spin Co^{3+} states above $T \sim 200\,K$ and a metal-insulator transition at $T \sim 600\,K$ [12]. The magnetic properties of $PrCoO_3$ were influenced by the hybridisation of 4f states of Pr^{3+} with the electronic valence states. Thermal conductivity in fact depends on the phonon scattering mechanism and the crystal field splitting of Pr^{3+}4f levels. The difference in the ionic radii of LS and excited states of Co^{3+} ions, with larger and smaller ionic radii causes disorder in the lattice and disturbs the scattering of phonons [13]. Sr, Ba and Ca substituted $PrCoO_3$ compounds, due to the double exchange mechanism between Co ions, exhibit the phenomenon of ferromagnetism well below $T \sim 280\,K$ [14]. The double exchange mechanism shown by Zener gives an explanation for the process that is involved in magnetic transitions [15]. Doping of alkaline earth metals, increases the hole concentration and creates the nanosized clusters will grow in size and multiply in number. These clusters trigger antiferromagnetic as well as ferromagnetic exchange interactions resulting in spin glass behaviour even below the magnetic ordering temperature. In these compounds electrical conductivity as well as oxygen ion conductivity were enhanced due to the oxidation of Co^{3+} to Co^{4+} and the formation of oxygen vacancies [16].

These materials have a lot of other applications as catalysts for effluent gas treatment, CO oxidation, esterification, methane oxidation, gas sensors and in solid oxide fuel cells. It was observed that in $PrCo_{1-x}Mg_xO_3$ compounds, with doping above $x = 0.1$ in Co site, Mg increases the formation of Co^{4+} ions and enhances the number of oxygen vacancies, so the electrical conductivity increases. But for a certain limit $x > 0.2$, due to the segregation of Pr_6O_{11}, blocking of oxygen transport occurs resulting in the decrease of electrical conductivity [17]. Tomes *et al.* [18] studied the transport and magnetic properties of Ni substituted $PrCoO_3$. The lattice parameters and hence the unit cell volume increases with Ni content due the larger ionic radii and it stabilises IS in the LS cobalt matrix. For Ni content $0.07 \leq x \leq 0.29$, it shows insulating behaviour, thermal conductivity decreases with increase in Ni content and spin-glass behaviour in those compounds exists [18]. Asamoto *et al.* [19] studied the catalytic activity of $PrCo_{1-x}Fe_xO_3$ for Carbon monoxide oxidation.

In this study, complex impedance spectrum analysis is employed for the characterisation of microstructures and electrical properties of ceramic oxides. The complex impedance Z^*, can be expressed as:

$$Z^* = Z' - j \cdot Z'' \tag{1}$$

$$Z' = \frac{R}{(1 + \omega RC)^2} \tag{2}$$

$$Z'' = \frac{R \cdot (\omega RC)}{(1 + \omega RC)^2} \tag{3}$$

where Z' and Z'' are real and imaginary components of impedance, R and C are resistance and capacitance and ω the angular frequency. The Z' versus Z'' gives the impedance plot called Nyquist plot which are used for the characterisation of interfacial, grain boundary and bulk grain effects. Impedance spectroscopy has been successfully applied in the investigation of relaxation process and the dielectric behaviour and can be well explained by Maxwell-Wagner model [20,21].

This report is unique in such a way that the nanopowders of Bi and Sr substituted $PrCo_{0.6}Fe_{0.4}O_3$ perovskites were successfully synthesised by a polymer precursor method, citrate sol-gel auto-combustion method [22]. The electrical conductivity and the impedance measurements were carried out for studying the conduction mechanism and the relaxation process which was not done so far. We have under taken the data of impedance, electric modulus, conductivity and the dielectric constant simultaneously for the study of AC conductivity mechanisms. Bi can change the electric, magnetic and thermoelectric properties with the assumption that it has a lone electron pair arising from the hybridisation of 6s and 6p atomic orbitals with $6s^2$ electrons. On the other hand, Sr can create oxygen vacancies which enhance the conductivity [23,24].

II. Experimental procedure

The samples $PrCo_{0.6}Fe_{0.4}O_3$ (P0), $Pr_{0.9}Bi_{0.1}Co_{0.6}Fe_{0.4}O_3$ (P1), $Pr_{0.8}Bi_{0.2}Co_{0.6}Fe_{0.4}O_3$ (P2) and $Pr_{0.8}Bi_{0.1}Sr_{0.1}Co_{0.6}Fe_{0.4}O_3$ (P3) were synthesized by citrate sol-gel auto-combustion method. The doping was carried out by dissolving $Pr(NO_3)_3 \times 6\,H_2O$, $Co(NO_3)_2 \times 6\,H_2O$, $Fe(NO_3)_3 \times 9\,H_2O$, $Bi(NO_3)_3 \times 9\,H_2O$, $Sr(NO_3)_2$, citric acid and ethylene glycol (all Sigma Aldrich 99.99–99% purity) in concentrated nitric acid and deionised water. The mixed solutions were heated and stirred to form polymer complex. Further heating of solutions leads to decomposition followed by auto-combustion to fine heaps of powders. The final products were calcined at 700 °C for 6 h and grounded using agate mortar and pestle. The powders were pelleted as circular disc with 10 mm diameter with a pressure of 2–3 tons and sintered at 900 °C for 8 h. The resulting powders and pellets were subjected to different characterization techniques to elucidate its internal structure and physical properties.

The crystal structure of the prepared samples was confirmed by X-ray diffraction studies (Rigaku Miniflex 600, with scan rate 1°/min and Cu-Kα radiation, $\lambda = 1.5418$ Å). The morphology and chemical composition were characterized and analysed by scanning elec-

tron microscopy, SEM (Carl Zeiss Ultra 55 FE-SEM) equipped with energy dispersive X-ray spectrometer (EDS). The X-ray photoelectron spectra (XPS) were measured for the bulk samples with MgKα source with excitation energy of 1253.68 eV using Axis Ultra DLD Kratos. The AC impedance measurements and the dielectric properties at room temperature were carried out using TFA 2000 AC impedance analyser in the frequency range from $1 < f < 10^6$ Hz.

III. Results and discussion

3.1. Structural characterization

The XRD patterns of the sintered P0, P1, P2 and P3 samples were shown in Fig. 1. The results show that crystallographic phases of single and double substituted perovskites belong to the standard crystallographic structure of orthorhombic $PrCoO_3$ (ICDD No. 01-078-3155) with *Pbnm* space group. The presence of secondary peaks is visible only in the sample P2 ($Pr_{0.8}Bi_{0.2}Co_{0.6}Fe_{0.4}O_3$). Lattice parameters were obtained using PDXL-software and tabulated in Table 1. The sharp XRD peaks confirm the formation of highly crystalline phases and the crystallite size was calculated using Scherer formula:

$$t = \frac{\kappa \cdot \lambda}{\beta \cdot \cos\theta} \qquad (4)$$

where κ depends on the shape of crystallite size ($\kappa = 0.9$, for spherical grains), λ is the X-ray wavelength, and β

is the full width at half maximum of the most intense peak. The samples P1 and P3 have somewhat higher values of lattice parameters than the pure $PrCo_{0.6}Fe_{0.4}O_3$, due to the doping with smaller amount of Bi and Sr, and both samples obey Vigard's law. However, the sample P2 ($Pr_{0.8}Bi_{0.2}Co_{0.6}Fe_{0.4}O_3$) has the presence of secondary peak due to the crossing of solubility limit of Bi in the crystal lattice [25]. Goldschmidt formula was used for calculating the tolerance factor [26].
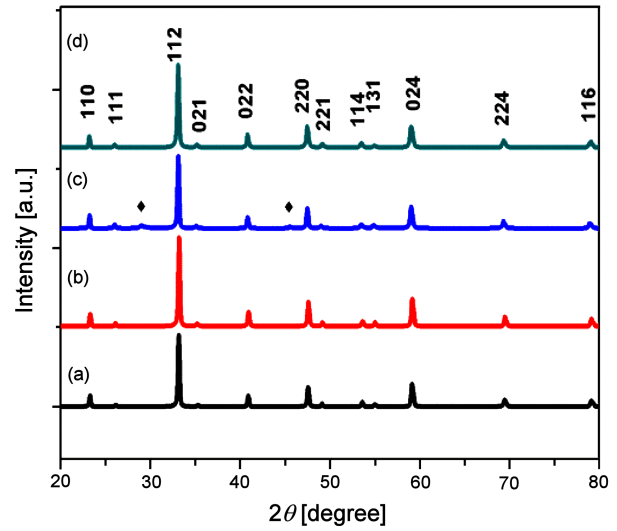
Figure 1. XRD patterns of samples sintered at 900 °C for 8 h: a) P0, b) P1, c) P2 and d) P3
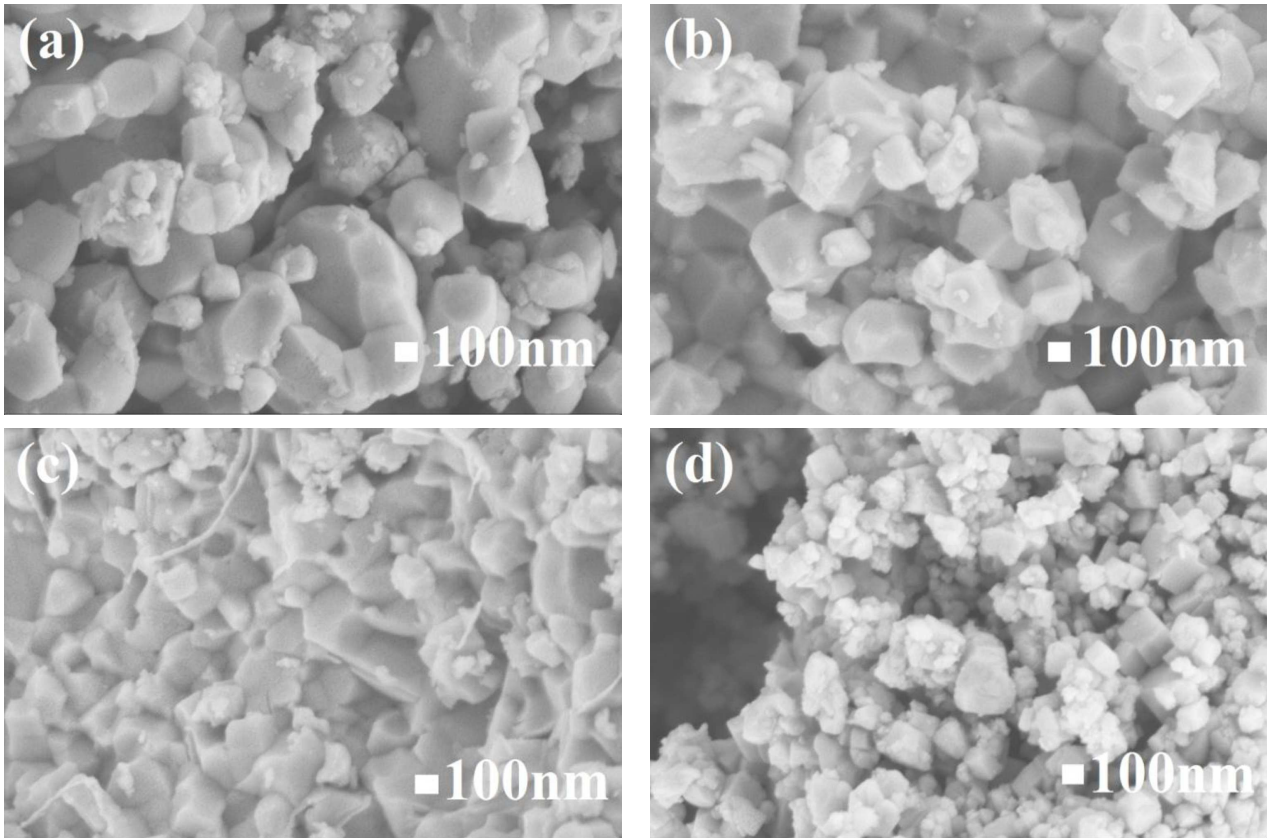
Figure 2. SEM micrographs of ceramics sintered at 900 °C for 8 h: a) P0, b) P1, c) P2 and d) P3

Table 1. Lattice parameters, volume, tolerance factor and crystallite size of single and doubly substituted $PrCo_{0.6}Fe_{0.4}O_3$

Sample	Lattice parameters ±0.001 Å			Volume [Å³]	Tolerance factor	Crystallite size [nm]
	a [Å]	b [Å]	c [Å]			
$PrCo_{0.6}Fe_{0.4}O_3$ (P0)	5.4176	5.3962	7.6405	295.9072	0.967	46.4
$Pr_{0.9}Bi_{0.1}Co_{0.6}Fe_{0.4}O_3$ (P1)	5.4363	5.3995	7.6490	295.9072	0.957	46.1
$Pr_{0.8}Bi_{0.2}Co_{0.6}Fe_{0.4}O_3$ (P2)	5.4127	5.3977	7.6313	295.9086	0.948	44.5
$Pr_{0.8}Bi_{0.1}Sr_{0.1}Co_{0.6}Fe_{0.4}O_3$ (P3)	5.4252	5.4061	7.6510	295.9072	0.962	42.9

The SEM images and EDS spectra of the prepared samples are shown in Fig. 2. As it can be seen the average grain size is in range from 200–400 nm and decreases with Bi and Sr doping. At high temperatures Bi acts as grain growth inhibitor and increases sinterability [27]. The energy dispersive X-ray spectroscopy (EDS) analyses confirm the presence of Bi and Sr in the doped samples.

The XPS spectra of P0, P1, P2 and P3 are recorded to determine the valence states of Pr, Bi, Sr, Co and Fe ion. The binding energies values of each element were tabulated in Table 2. The Pr-3d core level spectra of P0, P1, P2 and P3 are shown in Fig. 3. It is observed that Pr-3d has the presence of doublet line with $3d_{3/2}$ and $3d_{5/2}$ peaks at 953 eV and 933 eV. The splitting of Pr-3d peaks are due to the coupling of 3d and 4f hole states [28]. The observed binding energy splitting of 4.5 ± 0.2 eV is in good agreement with the data reported by Pandey *et al.* [29]. The exchange splitting of 3d in Pr is 20 ± 0.2 eV. The peak positions vary only by ± 0.2 eV for all samples, independent on Bi and Sr substitution, indicating Pr^{3+} as predominant oxidation state in all samples. All other elements were fitted in accordance to our previous results [30]. The oxidation state of Bi, Co and Fe were found to be +3. The presence of satellite peaks in Co and Fe indicates the existence of Co^{2+} and Fe^{2+} ions in the compounds. The oxidation state of Sr was found

Table 2. XPS peak positions (binding energy) of elements

Sample	Binding energy [eV]			
	P0	P1	P2	P3
Pr-$3d_{3/2}$	953.3	953	953.1	953.1
	948.7	948.6	948.8	948.6
Pr-$3d_{5/2}$	933.2	932.8	932.9	932.9
	929	928.6	928.5	928.6
Bi-$4f_{5/2}$		164.6	164.4	164.5
		164	164	164.3
Bi-$4f_{7/2}$		159.1	159	159.1
		158.7	158.6	159
Sr-$3d_{3/2}$				134.1
Sr-$3d_{5/2}$				132.6
Co-$2p_{1/2}$	795.5	795.3	795.2	795.3
Co-$2p_{3/2}$	780.3	780.1	780.1	780.1
Co-satellite	788.6	788.5	788.9	787.6
Fe-$2p_{1/2}$	724	724	724	723.8
Fe-$2p_{3/2}$	710.7	710.6	710.1	710.3
Fe-satellite	714.5	715	712	712.8
O-1s	531.5	531.1	531.2	531.3
	529.3	529.2	529.3	529.2
O_A/O_L	0.98	0.86	0.49	1.1
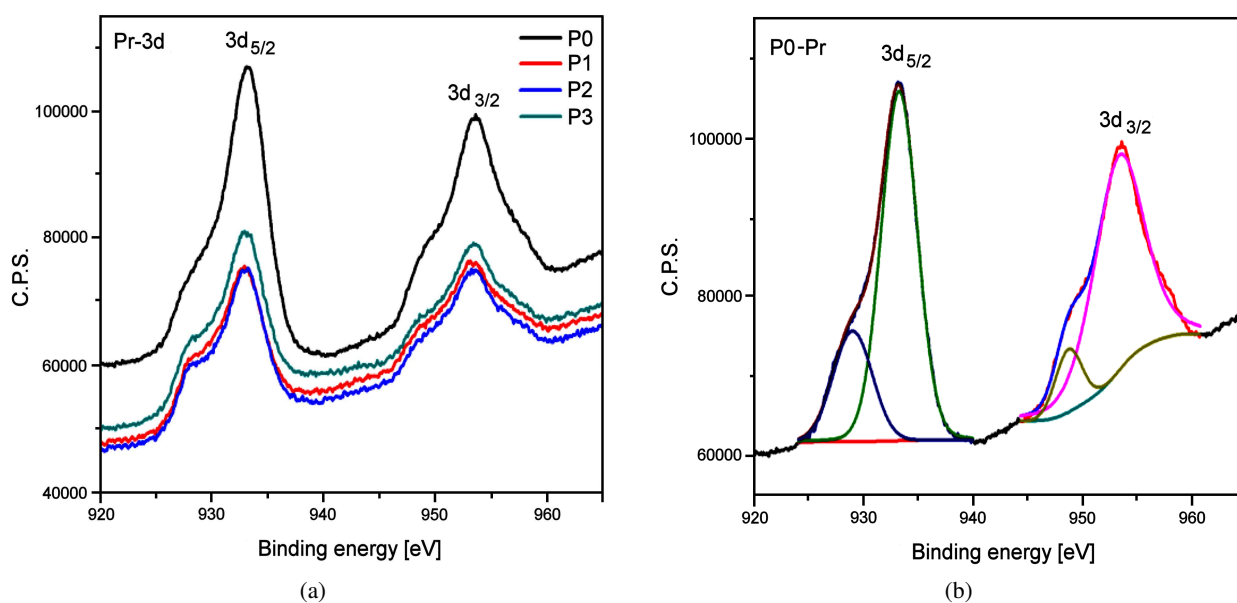
Figure 3. XPS spectra of: a) Pr-3d for samples P0, P1, P2 and P3; and b) peak fitting of Pr for sample P0
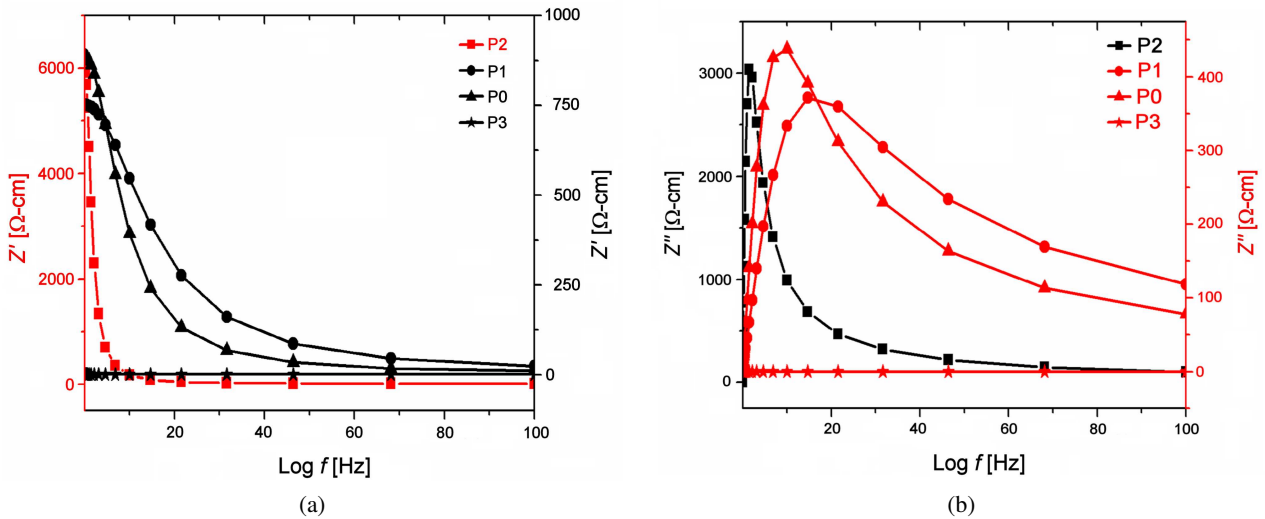
Figure 4. The variation of Z′ (a) and Z″ (b) with frequency at room temperature

to be +2. There is only a slight shift in binding energy values due to the doping with Bi and Sr without changing the oxidation state of other elements. The number of oxygen vacancies was calculated from the ratio of the adsorbed oxygen to the lattice oxygen present in the samples and was found to be more in Sr doped sample P3.

3.2. Electrical properties

The variations of $Z′$ and $Z″$ with frequency at room temperature are shown in Fig. 4. The value of $Z′$ decreases monotonically with increase in frequency and reached a constant value at high frequency in all samples due to the space charge polarization effects. The ceramics P2 has larger impedance value than other samples due to the presence of secondary phase while the P3 does not have significant impedance at room temperature.

In the variation of $Z″$ with frequency plot, there is a clear evidence of appearance of a peak and typical peak broadening for the samples P0, P1 and P2. The appearance of the peak indicates the existence of relax-

ation process and the peak formation occurs when the hopping frequency of the localised electrons becomes in the order of frequency of the applied field. The asymmetric peak broadening indicates the spreading of relaxation times. A large effect of polarization is seen in these compounds [31,32].

The Nyquist plot is drawn to study the effect of electrode, grain and grain boundary on the impedance (Fig. 5). Equivalent circuit of $R1(R2 \cdot C)$ configuration is used as a model. Only one semicircle is obtained and the capacitance value is in nanofarads, which indicates the grain boundary resistance dominating over grain resistance at room temperature [33]. Since the ceramics P3 does not have significant impedance at room temperature, the corresponding Nyquist plot was not presented. By fitting the curve using Z-view software, the circuit parameters are obtained and tabulated in Table 3 with an error of ±5%. In the used equivalent circuit, $R1$ is the contact resistance, which is very small compared to the grain boundary resistance ($R2 = R_{gb}$) and C is the capacitance of the grain boundary ($C = C_{gb}$). The increase in size of semicircular arcs with doping is at-
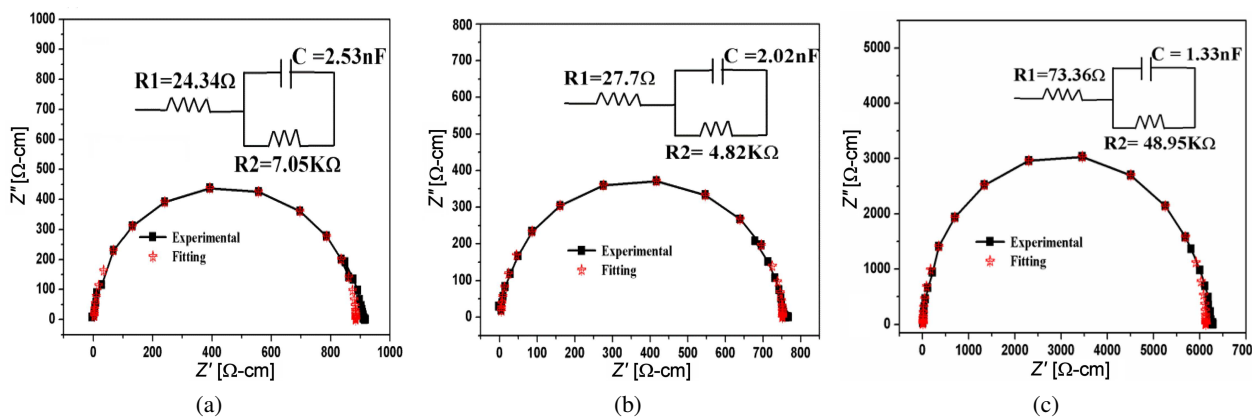
Figure 5. Nyquist plot for samples: a) P0, b) P1 and c) P2, at room temperature with the equivalent circuits

(a)

(b)
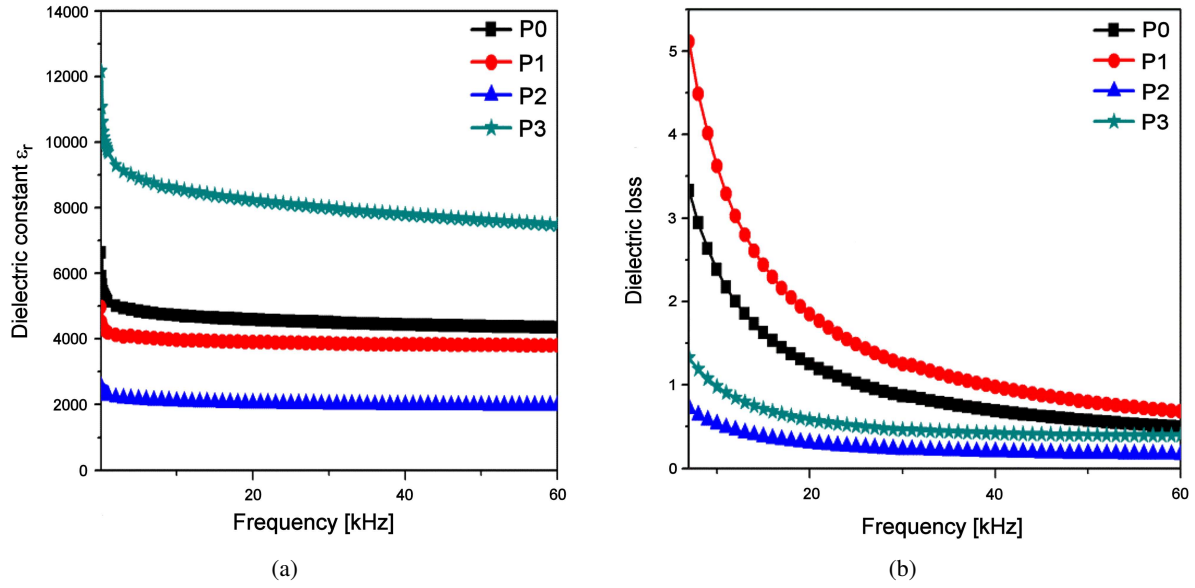
Figure 6. Frequency dependence of dielectric constant and dielectric loss for samples P0, P1, P2 and P3

Table 3. Equivalent circuit parameters from Nyquist plot

Sample	$R1$ [Ω]	$R2$ [kΩ]	C [nF]	τ [10^{-6} s]	f_{max} [kHz]
P0	24.34	7.05	2.53	17.84	8.92
P1	27.7	4.82	2.02	9.74	16.35
P2	73.36	48.95	1.33	65.10	2.45

tributed to the increase in resistance of the corresponding components in the sample. The sample P2 has high grain boundary resistance due to the presence of the secondary phase. The *R-C* parallel circuit has a relaxation with time constant τ, which can be obtained using the following equations:

$$\tau = R_{gb} \cdot x \cdot C_{gb} \qquad (5)$$

$$2\pi \cdot f_{max} \cdot \tau = 1 \qquad (6)$$

The variation of dielectric constant and dielectric loss with frequency is shown in Fig. 6. The samples exhibit large dielectric permittivity and loss at low frequency and their decrease with increasing frequency, which is the normal dispersion behaviour of semiconducting oxides. The decrease in dielectric constant with frequency can be due to the contribution of the multi-component polarizability, i.e. deformational and relaxation. As frequency increases dipoles are no longer able to rotate and their oscillation begins to lag behind the field, so dielectric constant approaches limiting value. For the sample P1, higher value of tan δ was observed due to the increases in DC conductivity of the material [34].

The frequency dependent AC conductivity at room temperature is shown in Fig. 7. It presents a power law behaviour at high frequency region. In such cases Jonscher's empirical formula termed as universal dielectric response (UDR) was used for explaining the AC con-

duction mechanism. By UDR law, the total electrical conductivity can be written as:

$$\sigma(\omega) = \sigma_{DC} + \sigma_0 \cdot f^s \qquad s \le 1 \qquad (7)$$

where *s* is the frequency exponent, σ_{DC} is the DC bulk conductivity and σ_0 is a constant. The UDR behaviour can originate from different source. The one due to the presence of defects and disorder causes electron hopping or tunnelling through energy barriers between localised states. Another originates from extrinsic effects like contacts, grain boundary etc. Here up to the frequency region of 10 Hz to 10 kHz the conductivity stayed constant due to the free charge formation. The conductivity increases linearly with increasing frequency above 10 kHz as in the disordered materials. At high frequency UDR to Super linear power law (SLPL) behaviour was seen, due to the polaron hopping mechanism. The hopping of charge carriers between localised states occurred in disordered system due to the grain
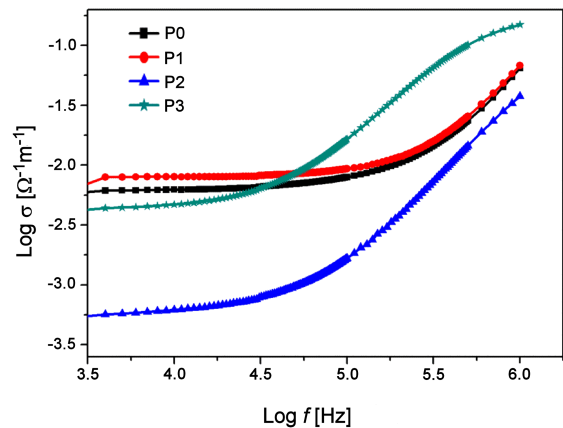
Figure 7. Frequency (*f*) dependence for AC conductivity of samples P0, P1, P2 and P3 at room temperature

(a)　　　　　　　　　　　　　　　　(b)
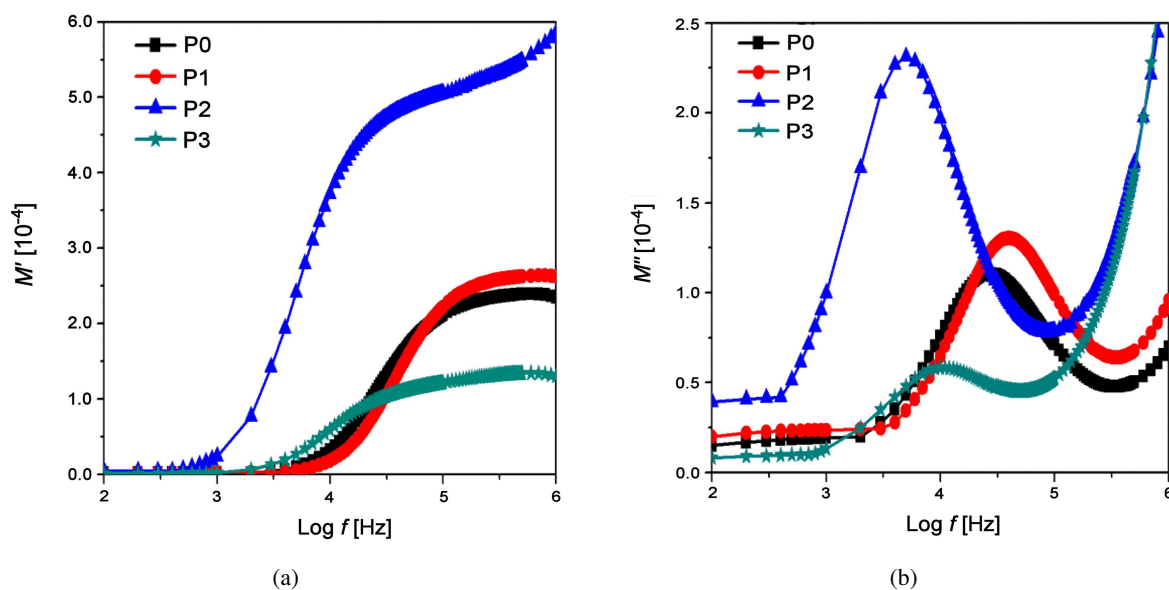
Figure 8. Modulus plots: a) M' and b) M'' for samples P0, P1, P2 and P3

boundary effect. The sample P2 has lower conductivity due to the presence of secondary phase and high grain boundary resistance value. The sample P1 has somewhat higher conductivity than the P0, which is complementary to the obtained impedance data, whereas the sample P3 is material with the highest conductivity [35].

For understanding the relaxation process, we have calculated a parameter called electrical modulus, which is reciprocal value of complex relative permittivity. Figure 8 shows the real (M') and imaginary (M'') part of electrical modulus as the function of logarithmic frequency. Above 1 kHz M' and M'' are frequency dependent. The variation of M'' with frequency provides information of the charge transport mechanism, such as electrical transport, conductivity, relaxation etc. Peaks observed in spectra indicate the existence of conductivity relaxation process. According to Maxwell-Wagner model, combined dielectric and electric modulus measurements explain the effect of large grain boundaries on the electrical conduction mechanism. By this theorem, the dielectric medium is made of well conducting grains with poorly conducting or resistive grain boundary responsible for the relaxation process. At low frequency, small conductivity of grain boundary contributed to the high dielectric constant. The relaxation peak of the sample P2 is shifted to the low frequency region due to the presence of the secondary phase and high grain boundary effect. Due to the less resistive walls, the P3 material has high value of conductivity [36].

IV. Conclusions

The $Pr_{1-x}Bi_xCo_{0.6}Fe_{0.4}O_3$ ($x = 0$, 0.1, 0.2) and $Pr_{0.8}Bi_{0.1}Sr_{0.1}Co_{0.6}Fe_{0.4}O_3$ perovskite ceramics were successfully prepared by citrate sol-gel auto-combustion method and sintered at 900 °C. All

compounds have orthorhombic crystal structure with *Pbnm* space group, and a small amount of secondary phase was observed only in the sample with higher Bi content ($Pr_{0.8}Bi_{0.2}Co_{0.6}Fe_{0.4}O_3$). The grains of the sintered materials have size of few hundred of nanometres. It was clear from SEM that, by the substitution of Bi and Sr the grain size decreases. The EDS result confirms the elemental composition. From XPS predominant oxidation state of Pr, Bi, Co and Fe are found to be +3 and for Sr this is +2. The impedance data analysis reveals that, at room temperature the grain boundary resistance is dominant. The sample $Pr_{0.8}Bi_{0.2}Co_{0.6}Fe_{0.4}O_3$ has high value of impedance. Two distinct values for dielectric constant at low and high frequency and also the asymmetric modulus behaviour indicated the existence of relaxation process. For the sample $Pr_{0.8}Bi_{0.2}Co_{0.6}Fe_{0.4}O_3$ due to the highly resistive grain boundary wall, the conductivity decreases. Anomalous behaviour at high frequency indicates the presence of defects or lack of periodicity. The processes of relaxation in Bi and Sr doped ceramics were well explained by Maxwell-Wagner model. The $Pr_{0.8}Bi_{0.1}Sr_{0.1}Co_{0.6}Fe_{0.4}O_3$ has low impedance and is highly conductive materials.

References

1. G. Murtaza, I. Ahmad, B. Amin, A. Afaq, M. Maqbool, J. Maqssod, I. Khan, M. Zhahid, "Investigation of structural and optoelectronic properties of BaThO$_3$", *Opt. Mater.*, **33** (2011) 553–557.
2. H. Wang, G. Li, L. Li, "Molten-salt-mediated synthesis

and low-temperature electrical conduction of LnCoO$_3$ (Ln = Pr, Nd, Sm, and Gd)", *J. Alloys. Compd.*, **612** (2014) 227–232.

3. M. Imad, A. Fujimori, Y. Tokura, "Metal-insulator transitions", *Rev. Mod. Phys.*, **70** (1998) 1039–1263.

4. P.M. Raccah, J.B. Goodenough, "First-order localized-electron $\leftrightarrows$ collective-electron transition in LaCoO$_3$", *Phys. Rev.*, **155** (1967) 932–943.

5. S. Yamaguchi, Y. Okiomoto, H. Taniguchi, Y. Tokura, "Spin-state transition and high-spin polarons in LaCoO$_3$", *Phys. Rev. B*, **53** (1996) 2926–2929.

6. J.M.D. Coey, M. Viret, S.V. Molnaacuter, "Mixed-valence manganites". *Adv. Phys.*, **48** (1999) 167–293.

7. K. Yoshii, H. Abe, A. Nakamura, "Magnetism and transport of Ln$_{0.5}$Sr$_{0.5}$CoO$_3$ (Ln = Pr, Nd, Sm and Eu)", *Mater. Res. Bull.*, **36** (2001) 1447–1454.

8. M.A. Senaris Rodriguez, J.B Goodenough, "Magnetic and transport properties of the system La$_{1-x}$Sr$_x$CoO$_{3-\delta}$ ($0 < x \leq 0.50$)", *J. Solid State Chem.*, **118** (1995) 323–336.

9. I.O. Troyanchuk, D.V. Karpinskii, V.M. Dobryanskii, Yu.A. Fedotova, H. Szymczak, "The two-phase crystal structure and magnetic properties of the LaCo$_{1-x}$Fe$_x$O$_{3-d}$ system", *J. Exp. Theor. Phys.*, **100** (2005) 1121–1126.

10. D.V. Karpinskii, I.O. Troyanchuk, K. Barner, H. Szymczak, M. Tovar, "Crystal structure and magnetic ordering of the LaCo$_{1-x}$Fe$_x$O$_3$ system", *J. Phys.: Condens. Matter*, **17** (2005) 7219–7226.

11. M. Itoh, M. Mori, S. Yamaguchi, Y. Tokura, "NMR study of the spin state of RCoO$_3$ (R = Pr, Nd, Sm, and Eu)", *Physica B*, **259-261** (1999) 902–903.

12. K. Knizek, Z. Jirak, J. Hejtmanek, M. Veverka, M. Marysko, G. Maris, T.T.M. Palstra, "Structural anomalies associated with the electronic and spin transitions in LnCoO$_3$", *Eur. Phys. J.*, **47** (2005) 213–220.

13. G. Burns, "Shielding and crystal fields at rare earth ions", *Phys. Rev.*, **128** (1962) 2121–2130.

14. K. Yoshii, A. Nakamura, "Magnetic properties of Pr$_{1-x}$Sr$_x$CoO$_3$", *Physica B*, **281-282** (2000) 514–515.

15. P.W. Anderson, H. Hasegawa, "Considerations on double exchange", *Phys. Rev.*, **100** (1955) 675–681.

16. Z. Klencsar, Z. Nemeth, E. Kuzmann, Z. Homonnay, A. Vertes, J. Hakl, K. Vad, S. Meszaros, A. Simopoulos, E. Devlin, G. Kallias, J.M. Greneche, A. Cziraki, S.K. De, "The role of iron in the formation of the magnetic structure and related properties of La$_{0.8}$Sr$_{0.2}$Co$_{1-x}$Fe$_x$O$_3$ (x = 0.15, 0.2, 0.3)", *J. Magn. Magn. Mater.*, **320** (2008) 651–661.

17. Y. Ren, B. Li, J. Wang, X. Xu, "Synthesis and electrical conductivity of perovskite-type PrCo$_{1-x}$Mg$_x$O$_3$", *J. Solid State. Chem.*, **177** (2004) 3977–3980.

18. P. Tomes, M.H. Aguirre, R. Robert, A. Shkabko, E.H. Otal, A. Weidenkaff, "Transport and magnetic properties of PrCo$_{1-x}$Ni$_x$O$_3$ (x = 0.0–0.7)", *J. Phys. D: Appl. Phys.*, **44** (2011) 305402.

19. M. Asamoto, Y. Iwasaki, S. Yamaguchi, H. Yahiro, "Synthesis of perovsite-type oxide catalysts, Ln(Fe,Co)O$_3$ (Ln = La, Pr, Sm, Gd, Dy, Ho, Er, and Yb), from the thermal decomposition of the corresponding cyano complexes", *Catal. Today*, **185** (2012) 230–235.

20. J.R. Macdonald, *Impedance Spectroscopy*, Wiley, New York, 1987.

21. C. Sinclair, A.R. West, "Effect of atmosphere on the PTCR properties of BaTiO$_3$ ceramics", *J. Mater. Sci.*, **29** (1994) 6061–6068.

22. U. Megha, K. Shijina, G. Varghese, "Nanosized LaCo$_{0.6}$Fe$_{0.4}$O$_3$ perovskites synthesized by citrate sol gel auto combustion method", *Process. Appl. Ceram.*, **8** (2014) 87–92.

23. P. Ravindran, R. Vidya, A. Kjekshus, H. Fjellvag, O. Eriksson, "Theoretical investigation magnetoelectric behavior in BiFeO$_3$", *Phys. Rev. B*, **74** (2006) 224412.

24. D.S. Melo, E.P. Marinho, L.B. Soledade, D.A. Melo, S.G. Lima, E. Longo, I.M. Garcia Santos, A.G. Souza. "Lanthanum-based perovskites obtained by the polymeric precursor method", *J. Mater. Sci.*, **43** (2008) 551–556.

25. X. Liu, F. Gao, C. Tian, "Synthesis, low-temperature sintering and the dielectric properties of the ZnO–(1-x)TiO$_2$–xSnO$_2$ (x = 0.04–0.2)", *Mater. Res. Bull.*, **43** (2008) 693–699.

26. A. Kumar, A.S. Verma, S.R. Bhardwaj, "Prediction of formability in perovskite-type oxides", *Open Appl. Phys. J.*, **1** (2008) 11–19.

27. M. Adamczyk, Z. Ujma, L. Szymczak, A. Soszynski, J. Koperski, "Dielectric properties and relaxation of Bi-doped (Pb$_{0.75}$Ba$_{0.25}$)(Zr$_{0.70}$Ti$_{0.30}$)O$_3$ ceramics", *Mater. Sci. Eng. B*, **136** (2007) 170–176.

28. Y. Uwamino, T. Ishizuka, H. Yamatera, "X-ray photoelectron spectroscopy of rare-earth compounds", *J. Electron. Spectrosc. Relat. Phenom.*, **34** (1984) 67–78.

29. S.K. Pandey, R. Bindu, P. Bhatt, S.M. Chaudhari, A.V. Pimpale, "Synthesis and investigation of structural and electronic properties of Pr$_{1-x}$Ca$_x$FeO$_3$ ($0 \leq x \leq 0.2$) compounds", *Physica B*, **365** (2005) 47–54.

30. U. Megha, G. Varghese, K. Shijina, "Effect of Bi and Sr doping on morphological and magnetic properties of LaCo$_{0.6}$Fe$_{0.4}$O$_3$ nanosized perovskites", *Bull. Mater. Sci.*, **39** (2016) 125–131.

31. B.V. Bahuguna Sradhi, K. Srinivas, G. Prasad, S.V. Suryanarayana, T. Bhimasankaram, "Impedance spectroscopic studies in ferroelectric (Na$_{1/2}$Bi$_{1/2}$)TiO$_3$", *Mater. Sci. Eng. B*, **98** (2003) 10–16.

32. D.C. Sinclair, A.R. West, "Impedance and modulus spectroscopy of semiconducting BaTiO$_3$ showing positive temperature coefficient of resistance", *J. Appl. Phys.*, **66** (1989) 3850–3856.

33. M. Nadeem, M.J. Akhtar, A.Y. Khan, R. Shaheen, M.N. Haque, "AC study of 10% Fe-doped La$_{0.65}$Ca$_{0.35}$MnO$_3$ material by impedance spectroscopy", *Chem. Phys. Lett.*, **366** (2002) 433–439.

34. N.D. Sankir, E. Aydin, M. Sankir, "Impedance spectroscopy and dielectric properties of silver incorporated indium sulfide thin films", *Int. J. Electrochem. Sci.*, **9** (2014) 3864–3875.

35. P. Lunkenheimer, T. Gotzfried, R. Fichtl, S. Weber, T. Rudolf, A. Loidl, A. Reller, S.G. Ebbinghaus, "Apparent giant dielectric constants, dielectric relaxation and ac-conductivity of hexagonal perovskites La$_{1.2}$Sr$_{2.7}$BO$_{7.33}$ (B = Ru, Ir)", *J. Solid State Chem.*, **179** (2006) 3965–3973.

36. J. Liu, C.-G. Duan, W.-G. Yin, W.N. Mei, R.W. Smith, "Large dielectric constant and Maxwell-Wagner relaxation in Bi$_{2/3}$Cu$_3$Ti$_4$O$_{12}$", *Phys. Rev. B*, **70** (2004) 144106.